

A MMT/HECTOSPEC REDSHIFT SURVEY OF 24 MICRON SOURCES IN THE *SPITZER* FIRST LOOK SURVEY¹

CASEY PAPOVICH², RICHARD COOL, DANIEL EISENSTEIN, EMERIC LE FLOC'H³, XIAOHUI FAN,
ROBERT C. KENNICUTT, JR.⁴, J. D. T. SMITH, G. H. RIEKE AND MARIANNE VESTERGAARD

Steward Observatory, University of Arizona, 933 North Cherry Avenue, Tucson, AZ 85721

ABSTRACT

We present a spectroscopic survey using the MMT/Hectospec fiber spectrograph of 24 μm sources selected with the *Spitzer* Space Telescope in the *Spitzer* First Look Survey. We report 1296 new redshifts for 24 μm sources, including 599 with $f_\nu(24\mu\text{m}) \geq 1$ mJy. Combined with 291 additional redshifts for sources from the Sloan Digital Sky Survey (SDSS), our observing program was highly efficient and is $\sim 90\%$ complete for $i \leq 21$ mag and $f_\nu(24\mu\text{m}) \geq 1$ mJy, and is 35% complete for $i \leq 20.5$ mag and $0.3 \text{ mJy} \leq f_\nu(24\mu\text{m}) < 1.0$ mJy. Our Hectospec survey includes 1078 and 168 objects spectroscopically classified as galaxies and QSOs, respectively. Combining the Hectospec and SDSS samples, we find 24 μm -selected galaxies to $z_{\text{gal}} \leq 0.98$ and QSOs to $z_{\text{QSO}} \leq 3.6$, with mean redshifts of $\langle z_{\text{gal}} \rangle = 0.27$ and $\langle z_{\text{QSO}} \rangle = 1.1$. As part of this publication, we include the redshift catalogs and the reduced spectra; these are also available through the NASA/IPAC Infrared Science Archive.⁵

Subject headings: galaxies: high-redshift — infrared: galaxies

1. Introduction

Observations with the Infrared (IR) Astronomical Satellite (*IRAS*) discovered that much of the bolometric emission associated with star-formation and active-galactic nuclei occurs in the thermal infrared. The analysis of *IRAS* sources indicated that most ($\simeq 70\%$) of the light emitted from local, normal galaxies comes at UV and optical wavelengths (e.g. Soifer & Neugebauer 1991). However, measurements of the IR background found that the total far-IR emission ($\lambda = 8 - 1000 \mu\text{m}$) of galaxies is comparable to that measured at UV and optical wavelengths (e.g., Hauser et al. 1998). Therefore, over the history of the Universe, roughly half of the photons from star formation or black-hole accretion processes are emitted at IR wavelengths (Elbaz et al. 2002; Dole et al. 2006). Subsequent studies of IR number counts from the Infrared

¹This work is based in part on observations made with the *Spitzer Space Telescope*, which is operated by the Jet Propulsion Laboratory, California Institute of Technology, under NASA contract 1407

²Spitzer Fellow; papovich@as.arizona.edu

³Also associated to Observatoire de Paris, GEPI, 92195 Meudon, France

⁴Current address: Institute of Astronomy, University of Cambridge, Madingley Road, Cambridge CB3 0HA, United Kingdom

⁵<http://irsa.ipac.caltech.edu/>

Space Observatory (*ISO*; Elbaz et al. 1999) and more recently from the *Spitzer* Space Telescope (Marleau et al. 2004; Papovich et al. 2004) showed that IR-luminous galaxies have evolved rapidly, implying that they are a much more common phenomenon at high redshifts.

Studying the increase in the IR-active phases of galaxies requires measuring the properties of these objects as a function of redshift. Observations at $24\ \mu\text{m}$ from the multiband imaging photometer for *Spitzer* (MIPS, Rieke et al. 2004) are particularly well suited for such studies. Soifer, Neugebauer, & Houck (1987) concluded that starburst galaxies radiate as much as $\sim 40\%$ of their luminosity in the mid-IR ($8\text{--}40\ \mu\text{m}$). The mid-IR emission from starforming galaxies correlates almost linearly with total IR luminosity over a range of galaxy type (e.g., Spinoglio et al. 1995; Roussel et al. 2001; Papovich & Bell 2002; Calzetti et al. 2005). The angular resolution of *Spitzer* at $24\ \mu\text{m}$ is roughly a factor of 3 and 7 better than that at 70 and $160\ \mu\text{m}$, respectively, allowing unambiguous source identification and probing the IR emission from many more sources than at the longer wavelengths. Already, early studies of *Spitzer* $24\ \mu\text{m}$ sources with photometric redshifts over relatively small fields ($\lesssim 0.5\ \text{sq. deg}$) indicate that the bright end of the IR luminosity function evolves strongly from $z \sim 0$ to 1 (Le Floc’h et al. 2005; Pérez-González et al. 2005).

To improve our understanding of the nature and evolution of IR-luminous phases of galaxies, we first need to construct large samples of objects with spectroscopic redshifts. In this paper, we publish the results of our survey with the MMT/Hectospec multi-fiber spectrograph in the *Spitzer* First Look Survey (FLS). We report new redshifts for 1296 objects selected in the *i*-band and at $24\ \mu\text{m}$ over $3.3\ \text{deg}^2$. Here we publish the catalogs and reduced, flux-calibrated spectra. We are currently using these spectroscopic data in conjunction with surveys in other fields to study the evolution of the IR-luminous galaxy population.

We organize this paper as follows. In § 2, we discuss the *Spitzer* FLS dataset, our $24\ \mu\text{m}$ catalog, and our spectroscopic target selection. In § 3 we describe the spectroscopic observations and data reduction. In § 4 we discuss the spectroscopic completeness of the catalog. In § 5 we present the Hectospec spectra and redshift catalog. In § 6 we summarize our results and discuss the redshift distribution of our sample of $24\ \mu\text{m}$ sources. All magnitudes in this paper correspond to the AB system (Oke & Gunn 1983), where $m_{\text{AB}} = 23.9 - 2.5 \log(f_\nu / 1\ \mu\text{Jy})$.

2. *Spitzer* First Look Survey

2.1. Overview

The *Spitzer* FLS was a service to the *Spitzer* user community, initiated as a Director’s Discretionary Time program. The program goal was to provide data over large areas in time to have an impact on early *Spitzer* studies and proposals. The FLS includes three components, described at <http://ssc.spitzer.caltech.edu/fls>. Here, we focus on the extragalactic component, whose field was chosen to have low Galactic background and to be in the *Spitzer* continuous viewing zone (CVZ) such that it would be observable shortly after the *Spitzer* in-orbit checkout regardless of launch date.

The *Spitzer* FLS overlaps with imaging and spectroscopic observations from the Sloan Digital Sky Survey (SDSS; York et al. 2000). We use the SDSS imaging data to identify objects in the *Spitzer*/MIPS data for spectroscopic follow-up.

2.2. MIPS 24 μm Observations and Data

Spitzer observed the FLS during December 2003 (PID: 26; PI: B. T. Soifer). The MIPS observations consisted of medium-speed scan maps (AORKEYS: 3863808, 3864064, 3864320, 3864576, 3864832, 3865088, 3865344, 3865600, 3865856, 3866112, 3866368, 3866624). These 24 μm data cover roughly a field of 4.4 deg² at a depth of 90 sec (the “Shallow”, or “Main” field). Subsequent deeper observations (450 sec) were taken over a smaller field (0.26 deg²; the “Verification” field), but those data were not available prior to our MMT/Hectospec run. Thus, we use only the shallower-depth data over the larger field of view. See Marleau et al. (2004) for more details of the MIPS 24 μm dataset.

We retrieved the raw *Spitzer*/MIPS 24 μm data from the *Spitzer* archive and reduced them using the Data Analysis Tool (DAT) designed by the MIPS Guaranteed Time Observers (GTOs; Gordon et al. 2005). The measured count rates were corrected for dark current, cosmic rays, and flux nonlinearities, and then normalized by flat fields appropriate for each MIPS scan-mirror position. Images were then mosaicked after correcting for geometric distortion with a final plate scale of 1".247 pixel⁻¹.

We constructed a catalog from the reduced and mosaicked 24 μm image using SExtractor (Bertin & Arnouts 1996); table 1 gives the main parameters. We measured photometry in circular apertures of radius 12".3. To convert these to total count rates, we applied an aperture correction of 1.172 based on a curve-of-growth analysis of the 24 μm point spread function (PSF), and we converted these to flux density using the current calibration factor.⁶ For our primary and secondary spectroscopic targets, we selected the relatively bright MIPS sources with $f_\nu(24\mu\text{m}) \geq 300 \mu\text{Jy}$ (see § 2.3) and required that sources come from regions of the image with exposure time greater than 80 sec. Aperture-photometry for these bright 24 μm objects is fairly robust. Using aperture photometry from SExtractor, Marleau et al. (2004) demonstrated that the scatter between 24 μm flux densities for objects in the overlap region between the FLS shallow and verification fields is less than $\approx 20\%$. Our tests on the shallow FLS 24 μm image show that in apertures of radius 12".3 the 1 σ flux uncertainty is $\simeq 120 \mu\text{Jy}$. Therefore, the photometric measurements for objects with $f_\nu(24\mu\text{m}) > 1 \text{ mJy}$ have high signal-to-noise ratios ($S/N \gtrsim 8$), although photometric uncertainties on objects with $f_\nu(24\mu\text{m}) \sim 0.3 \text{ mJy}$ are higher ($S/N \sim 2-3$). Note that the signal-to-noise ratios are significantly higher in the (smaller) isophotal detection apertures. The flux uncertainty of $\sim 120 \mu\text{Jy}$ discussed above is only on the measurement in the larger photometric apertures.

The depth of the MIPS 24 μm data for the FLS is comparable to those of the NOAO deep wide-field survey (NDWFS) in the constellation Boötes (e.g., Houck et al. 2005), for which the 24 μm data is roughly 80% complete for sources above 270 μJy (Papovich et al. 2004). Similarly, Marleau et al. (2004) estimate the 80% completeness for the FLS 24 μm data at 230 μJy . We expect a similar completeness level in the FLS 24 μm catalog used here. However, both Marleau et al. and Papovich et al. used aperture photometry weighted by the 24 μm PSF, providing more accurate photometry vis-à-vis simple aperture photometry especially for fainter sources (particularly, e.g., at $f_\nu(24\mu\text{m}) \lesssim 300 \mu\text{Jy}$; see Marleau et al.). Therefore, we expect more scatter in the catalog used here particularly at faint flux densities, reducing the overall catalog completeness (see also § 2.3). For this reason and owing to the higher photometric uncertainties discussed above, the accuracy of the 24 μm flux densities below $\lesssim 0.5 \text{ mJy}$ may be insufficient for some applications.

⁶See <http://ssc.spitzer.caltech.edu/mips/> for aperture corrections and calibration factors.

2.3. Spectroscopic Target Selection

We selected MIPS 24 μm sources from our catalog as spectroscopic targets using the SDSS i -band photometry (Stoughton et al. 2002). We matched the MIPS 24 μm sources to SDSS i -band objects from Data Release 2 (rerun 40–44, Abazajian et al. 2004) within a radius of $2''$ down to $i \leq 21$ mag,⁷ excluding objects saturated in SDSS. We used the combined-model (`cmodel`) magnitude for our i -band photometry. The SDSS fits seeing-convolved elliptical de Vaucouleurs and exponential models to the deblended images. The `cmodel` aperture goes one step further by finding the best non-negative linear combination of the two (de Vaucouleurs and exponential) best fit models. The parameter of this mixture is listed as `frac_deV` in the SDSS data releases. The `cmodel` flux is taken as this linear combination of the best-fit model fluxes. Tests have shown that this combination tracks the Petrosian magnitudes well but with improved performance for fainter and smaller objects (Abazajian et al. 2004).

The SDSS deblender algorithm does not typically separate sources closer than $\sim 2\text{--}4''$ (e.g., Pindor et al. 2003). Although the MIPS 24 μm PSF is $6''$ FWHM, source centroiding is accurate to $< 1''$. Therefore, we expect few cases where multiple SDSS sources lie within $2''$ of a 24 μm source. In fact, we find that there are only 10 MIPS sources with 2 SDSS associations ($< 0.3\%$ of the matched 24 μm –SDSS sample; no MIPS source has more than 2 associations in SDSS). In these cases, we associate the 24 μm source with both SDSS sources in our catalogs for completeness. In practice, we placed Hectospec fibers on only 2 of these 20 SDSS galaxies, both of which are Galactic stars. Therefore, the few 24 μm sources with multiple object associations in SDSS has a tiny impact on our survey. However, there may still be some cases where the 24 μm –matched SDSS source is not the true association (i.e., the true optical counterpart is fainter than the SDSS detection limit). Alternatively, it may also be that the separation between the SDSS optical counterpart and the 24 μm source is $> 2''$, as may be the case for nearby galaxies where the optical centroid is offset from the 24 μm centroid.

To target objects for spectroscopy, we constructed a three-tiered sample:

$$\begin{aligned} \text{Primary Sample,} & & f_\nu(24\mu\text{m}) \geq 1.0 \text{ mJy} & \text{ and } & i \leq 21 \text{ mag;} \\ \text{Secondary Sample,} & & 0.3 \text{ mJy} \leq f_\nu(24\mu\text{m}) < 1.0 \text{ mJy} & \text{ and } & i \leq 20.5 \text{ mag;} \\ \text{Tertiary Sample,} & & f_\nu(24\mu\text{m}) < 0.3 \text{ mJy} & \text{ and } & i \leq 20.5 \text{ mag.} \end{aligned} \tag{1}$$

We exclude all sources with SDSS $3''$ –aperture fiber magnitudes $r \leq 17$ mag; this removes stars brighter than about $r < 17.3$ but affects very few galaxies. This sample selection identified 1076 sources in the primary sample, 2296 sources in the secondary sample, and 2325 sources in the tertiary sample, corresponding to survey densities of 0.07, 0.14, and 0.15 arcmin^{−2} within the FLS shallow field, respectively. This is our parent sample for spectroscopy. Table 2 presents the astrometry and photometry from the SDSS and MIPS 24 μm data for the parent sample. Note that each object in the parent sample is assigned a unique ID number, in column (1) of table 3. These ID numbers are used in subsequent tables to identify the object in the spectroscopic catalogs. The target-flag values (column 9) identifies objects satisfying the primary (**Target Flag**=2), secondary (**Target Flag**=4), or tertiary sample (**Target Flag**=8), as well as calibration stars (**Target Flag**=1), and other objects ($z \sim 0.5$ red galaxies, and quasars; **Target Flag**=0). Note that objects in the tertiary sample and those with **Target Flag**=0 are primarily used to fill out the fiber configurations, and in general these samples are too sparse to be statistically useful.

⁷The SDSS is 95% complete at $i = 21.3$ mag (Abazajian et al. 2004). However, we matched 24 μm sources against SDSS sources selected in *any* band. In particular, the r band data is 95% complete to $r \leq 22.2$ mag (Abazajian et al. 2004), allowing robust faint object detection somewhat below the fiducial i -band 95% completeness limit, see e.g., figure 1.

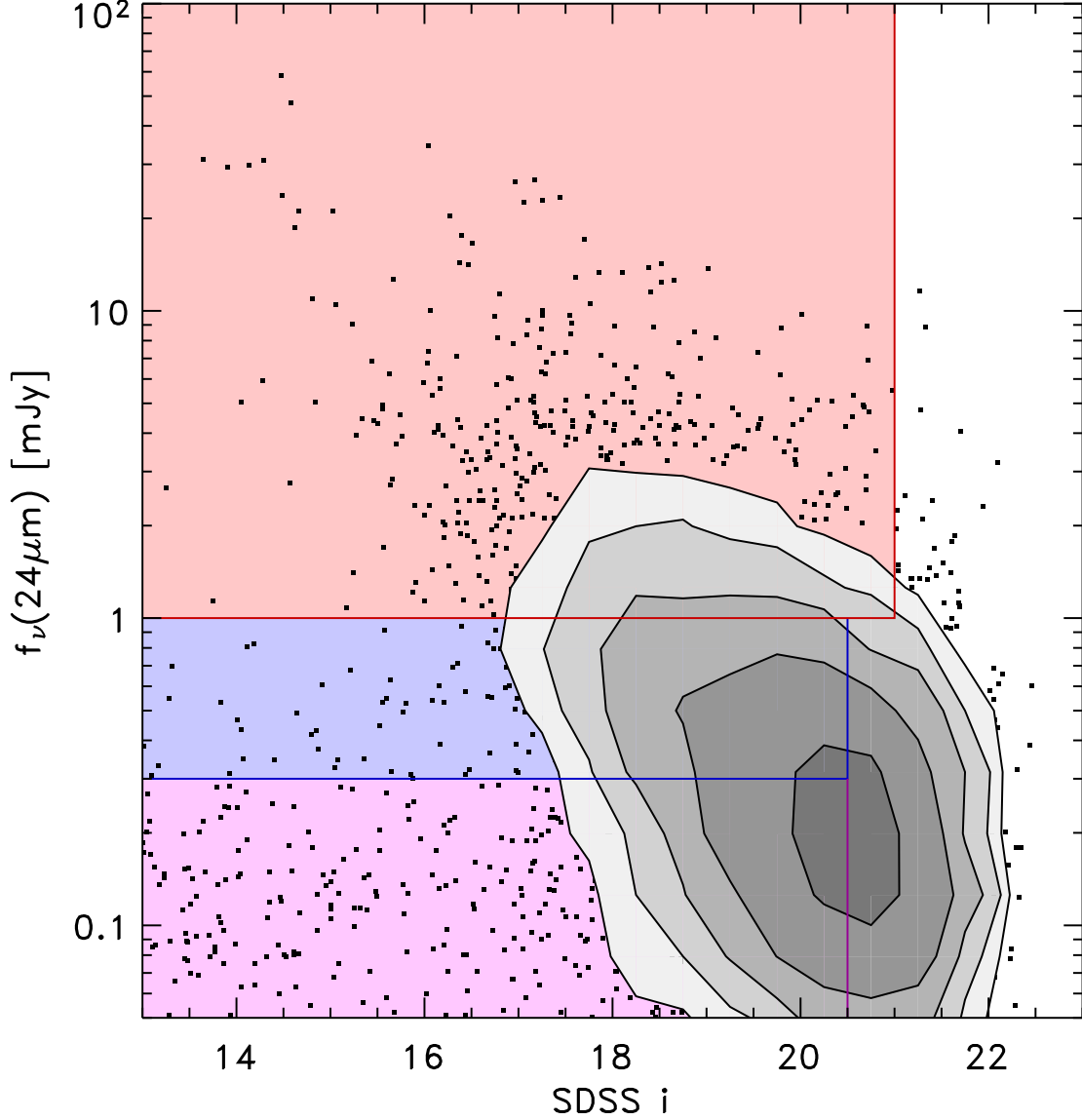


Fig. 1.— Distribution of $24\ \mu\text{m}$ flux densities of FLS sources as a function of SDSS i -band magnitude. We use contours where more than 16 data points fall in bins of $\Delta i = 0.5\ \text{mag}$ and $\Delta(\log f_\nu[24\mu\text{m}]) = 0.2\ \text{dex}$, and we plot individual points otherwise. The first contour corresponds to a source density of 16 objects in these bins, and each contour corresponds to a source density successively higher by a factor of two. Shaded rectangles show target selection for spectroscopy. The red-shaded region shows the primary selection, $f_\nu(24\mu\text{m}) \geq 1\ \text{mJy}$ and $i \leq 21\ \text{mag}$. The blue-shaded region shows the secondary selection, $0.3 \leq f_\nu(24\mu\text{m})/1\ \text{mJy} < 1$ and $i \leq 20.5\ \text{mag}$. The magenta-shaded region shows the tertiary selection, $f_\nu(24\mu\text{m}) < 0.3\ \text{mJy}$ and $i \leq 20.5\ \text{mag}$. Sources fainter than the $i \gtrsim 21.3\ \text{mag}$ will be missed in SDSS.

In figure 1 we illustrate our sample selection on a i -band magnitude versus $24\ \mu\text{m}$ flux-density diagram. For this plot, we show all MIPS $24\ \mu\text{m}$ sources with i -band counterparts, including sources with $i > 21$ mag in SDSS. The optical magnitude limit of our primary sample selection includes about 60% of all $24\ \mu\text{m}$ sources with flux densities above 1 mJy. We find that saturated stars (and objects blended with the light from saturated stars) account for 10% of sources with $f_\nu(24\mu\text{m}) \geq 1$ mJy, and a further 5% are galaxies where there exists a large centroiding offset between the optical and $24\ \mu\text{m}$ source or where the galaxy is split into multiple $24\ \mu\text{m}$ sources. The remaining 25% of the $f_\nu(24\mu\text{m}) \geq 1$ mJy population corresponds to objects with optical counterparts fainter than $i \gtrsim 21$ mag, likely similar to the IR-luminous galaxies and AGN at higher redshift ($z \gtrsim 1$) studied by Houck et al. (2005), Yan et al. (2005), and Weedman et al. (2006).

The distribution of *Spitzer* $24\ \mu\text{m}$ sources with fainter flux densities extends to fainter optical magnitudes. Thus, our survey is less complete for $24\ \mu\text{m}$ sources with $f_\nu(24\mu\text{m}) \leq 1$ mJy — we find that the optical magnitude limit of the secondary sample includes $\approx 32\%$ of all sources with $0.3\ \text{mJy} \leq f_\nu(24\mu\text{m}) < 1$ mJy in the Hectospec fields. This incompleteness is illustrated in figure 2, which shows the number counts of SDSS-matched $24\ \mu\text{m}$ sources. Compared with all $24\ \mu\text{m}$ sources in the Hectospec fields, the number distribution of SDSS-matched $24\ \mu\text{m}$ sources is mostly complete for $\gtrsim 1$ mJy, then begins to decline as the fraction of $24\ \mu\text{m}$ sources with SDSS-optical counterparts decreases. As a comparison, we show the expected number distribution of $24\ \mu\text{m}$ sources from the total number counts of Papovich et al. (2004).

SDSS provides spectroscopic coverage over the FLS field for objects with $r < 17.77$ mag. From the SDSS-matched $24\ \mu\text{m}$ catalog, 291 objects have spectroscopic redshifts from SDSS with no warnings on the redshift measurement (ZWARNING=0), split between stars (11), galaxies (223), and QSOs (57). We list the properties of these objects in table 4. ID numbers in column 1 of table 4 correspond to the ID numbers in column 1 of table 3. Because the objects in table 4 have high-quality redshifts and spectra from SDSS, we did not reobserve them with Hectospec.

3. Observations and Data Reduction

3.1. Observational Layout

Hectospec is a 300-fiber spectrograph covering a 1 degree-diameter field-of-view at the f/5 focus of the 6.5 m MMT (Fabricant et al. 2005). It began routine observing in 2004 April. Each fiber aperture is $1''.5$ diameter, and the resulting spectra cover a wavelength range of $\lambda = 3500 - 9000\ \text{\AA}$ with $6\ \text{\AA}$ FWHM resolution ($R \sim 1000$).

Figure 3 shows the *Spitzer* FLS layout including the locations of the Hectospec fields, the $24\ \mu\text{m}$ parent sample, and the $24\ \mu\text{m}$ sources with successfully measured redshifts. Each pointing provides some overlap with other pointings on the sky. The total area surveyed by the five Hectospec pointings is $3.3\ \text{deg}^2$, correcting for the overlap between the fields.

We generated FLS fiber configurations for five different fields, targeting sources from the parent sample defined in § 2.3. We named the configuration fields 131 to 135. We required that Hectospec place fibers on 4–7 spectrophotometric F-type stars selected from SDSS, and we placed ~ 30 fibers on blank-sky locations to measure the sky brightness. The remaining fibers (typically > 250) were placed on sources from the parent sample, giving the highest priority to objects in the primary sample, and lowest priority to objects in the tertiary sample. We executed our observations during 2004 July using an exposure time of 45 minutes split into 3×15 minute exposures. Seeing was typically sub-arcsecond. Table 2 summarizes the Hectospec field

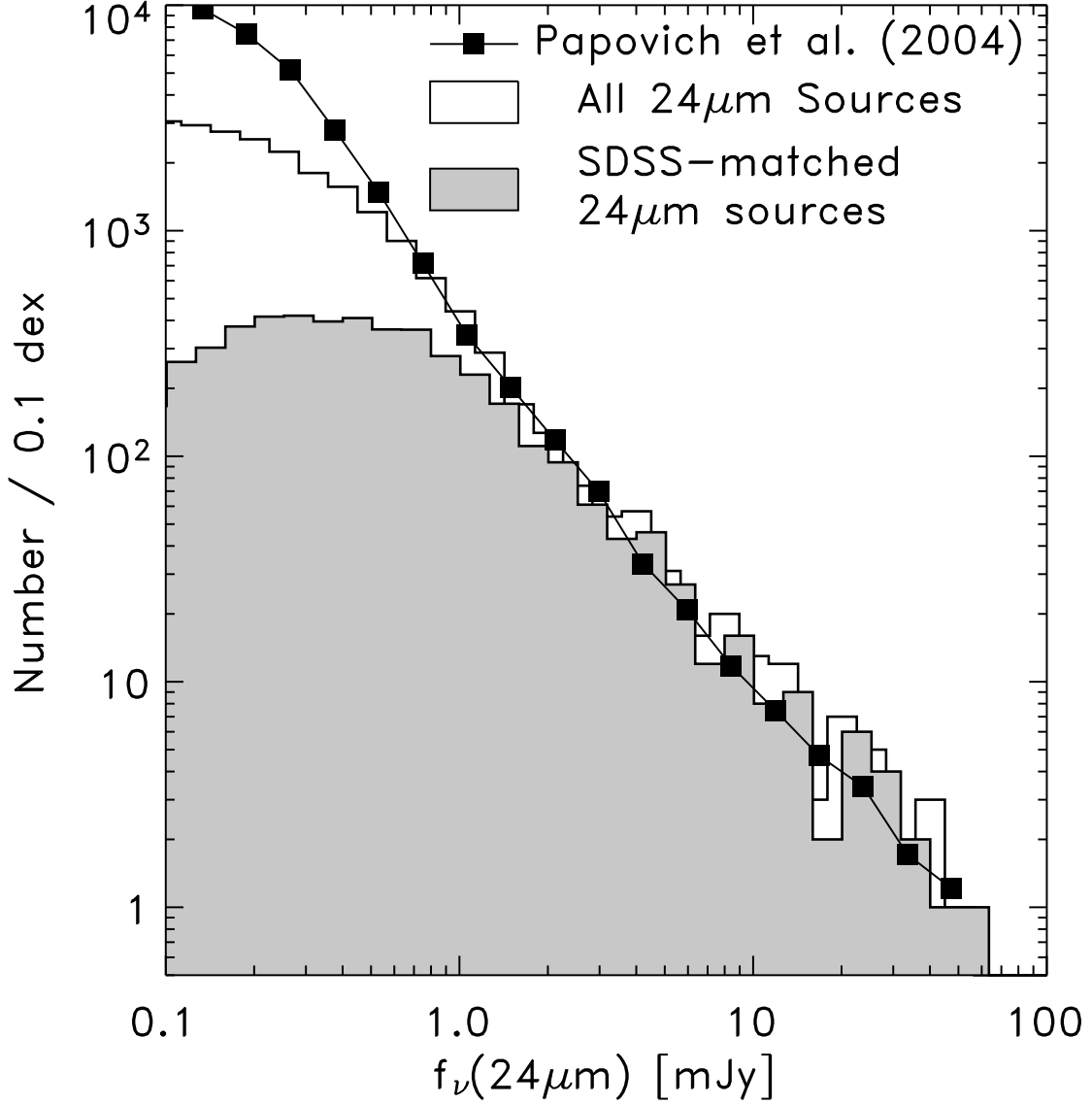


Fig. 2.— Number distribution of $24\ \mu\text{m}$ sources. The filled histogram shows the SDSS-matched $24\ \mu\text{m}$ sample in flux-density bins of 0.1 dex. The unfilled histogram shows the number distribution of all $24\ \mu\text{m}$ sources in the FLS that fall in the Hectospec fields. For comparison, the solid squares show the expected number distribution for $24\ \mu\text{m}$ sources based on the total number counts from Papovich et al. (2004), normalized to the area of the Hectospec survey ($3.3\ \text{deg}^2$). The drop in the number of SDSS-matched spectroscopic targets below $\sim 1\ \text{mJy}$ occurs because of the optical SDSS magnitude limit (see figure 1). The SDSS-matched sample excludes 40% of the $24\ \mu\text{m}$ sources with $f_\nu(24\ \mu\text{m}) > 1\ \text{mJy}$. Of these, $\sim 40\%$ are saturated stars and objects too close to saturated stars, nearby galaxies split into multiple $24\ \mu\text{m}$ sources, and objects with a large offset exists between the optical and $24\ \mu\text{m}$ source. The remaining objects (25% of the $f_\nu(24\ \mu\text{m}) \geq 1\ \text{mJy}$ population) have fainter optical counterparts, $i \gtrsim 21\ \text{mag}$.

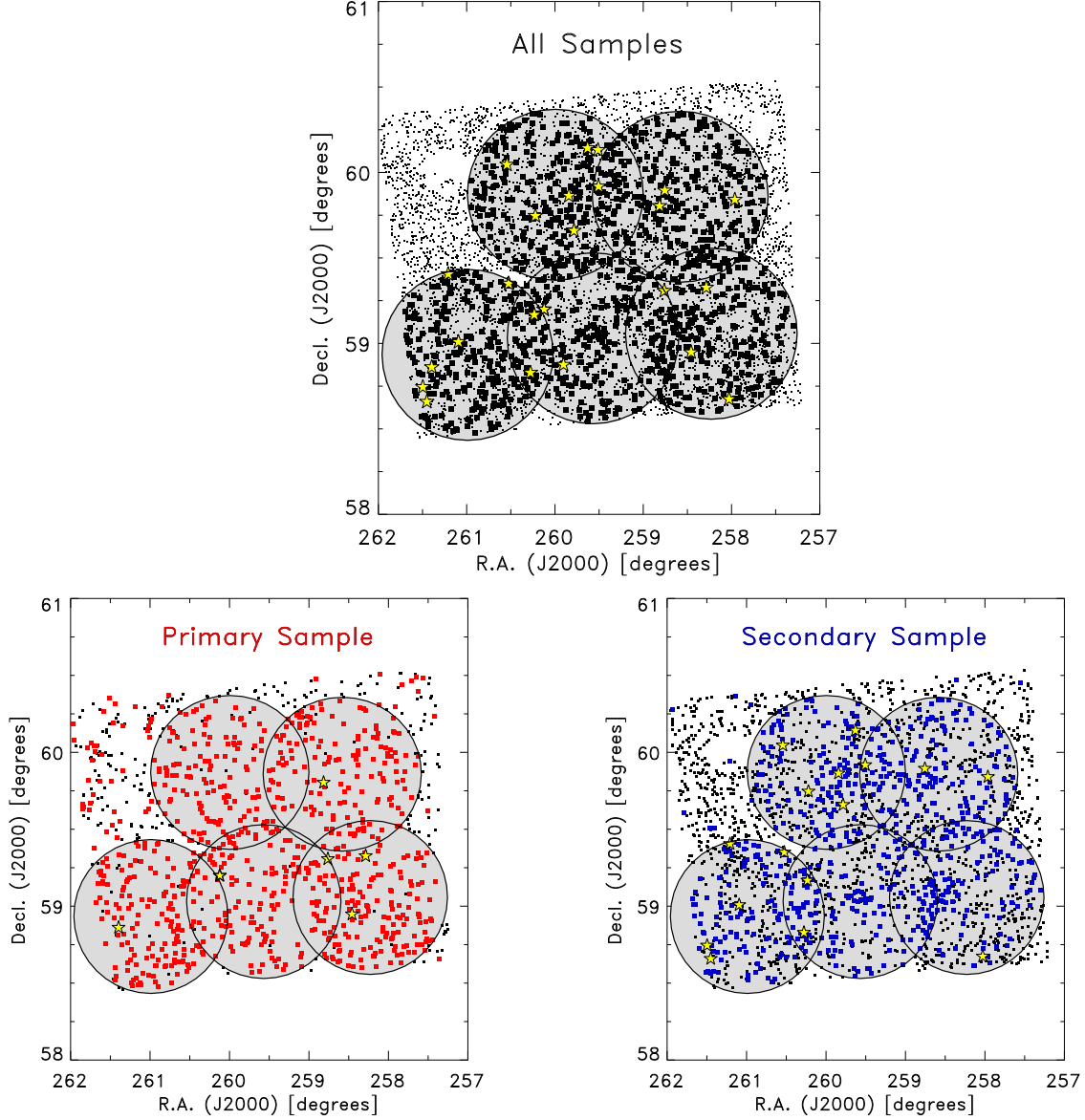


Fig. 3.— Hectospec field and SDSS-matched $24\ \mu\text{m}$ source locations in the *Spitzer* FLS. Large shaded circles show the positions of our Hectospec fields, also listed in table 2. The black dots in the top panel show objects from all three MIPS samples. Large, boxes show $24\ \mu\text{m}$ sources with successfully measured extragalactic redshifts from Hectospec only, yellow stars show sources spectroscopically classified as Galactic stars. The bottom panels show only those objects in the primary (1076 objects) and secondary samples (2296 objects), as labeled. In the bottom panels, the large, solid boxes show the 794 primary and 693 secondary sources with redshifts from either Hectospec or SDSS.

centers and log for the observations, including the airmass at the time of the observation. In total, we targeted 1291 sources for spectroscopy (605 primary targets, 632 secondary targets, 23 tertiary targets, and 31 filler targets); not including sky or unused fibers, nor calibration stars.

3.2. Data Reduction

We reduced the Hectospec data using HSRED⁸, an IDL package developed by one of us (R. Cool) for the reduction of data from the Hectospec and Hectochelle spectrographs (Fabricant et al. 2005; Szentgyorgyi et al. 1998). HSRED is based heavily on the reduction routines developed for SDSS. Initially, cosmic rays are identified and removed from the two-dimensional images using the IDL version of L. A. Cosmic (van Dokkum 2001) developed by J. Bloom. Dome flat observations are used to identify the 300 fiber traces on the two-dimensional images. These provide a high-frequency flat field and fringing correction for the object spectra. On nights when twilight sky spectra were obtained, these images were used to derive a low-order correction to the flat field vector for each fiber. We refine the wavelength solution for each observation, originally determined from HeNeAr comparison spectra, using the locations of bright sky lines in each object spectrum. We further use the strengths of several sky features to determine a small amplitude correction for each fiber to remove relative transmission differences between fibers, which are not fully removed by the flat field. The local sky spectrum for each observation is determined using the ~ 30 dedicated sky fibers, and is then subtracted from each object spectrum.

We flux-calibrate the spectra using simultaneous observations of the F-stars on each Hectospec configuration. The spectral class of each F-star is determined by a comparison against a grid of Kurucz (1993) atmospheric models. The ratio between the observed spectral shape of the F-star and the best fit model provides the shape of the sensitivity function of each fiber. SDSS photometric observations of the standard stars are used to normalize the absolute flux scale. After each exposure is extracted, corrected for heliocentric motion ($\approx 6 \text{ km s}^{-1}$, given the placement of the FLS in the *Spitzer* CVZ), and flux calibrated, we de-redden each spectrum according to the Galactic dust maps of Schlegel, Finkbeiner, & Davis (1998) using the O'Donnell (1994) extinction curve. Lastly, we coadd multiple exposures of a field to obtain the final, flux-calibrated spectra.

3.3. Problems with the Atmospheric Dispersion Corrector

Hectospec uses a counter-rotating atmospheric dispersion corrector (ADC) to counteract the atmosphere-induced wavelength-dependent aberration. Unfortunately, during the first few months of Hectospec operation (prior to 2004 October) the ADC was erroneously rotating in the wrong direction. As a result, our spectroscopic data suffer from double the usual wavelength aberration. As guiding is in the visual, light in the blue and red tend to miss the $1''.5$ -diameter fiber aperture, in an amount that depends on the surface brightness profile of the object. Point sources suffer more than extended ones.

As discussed in § 3.2, we attempted to flux-calibrate the spectra by matching the spectrophotometric F-type stars for each configuration to a grid of model atmospheres. Because of the atmospheric dispersion, the flux-calibration correction in the blue can be large, and for extended sources, it is typically overcorrected. Even point sources need not have the same calibration due to slight differences in the centroiding of the

⁸<http://mizar.as.arizona.edu/~rcool/hsred/>

target within the fiber. Figure 4 shows examples of several flux-calibrated spectra from our data from three different configurations, taken over the range of airmass 1.16–1.35 (see table 2). There is no way to correct for the problem with the ADC, so we do not recommend these data for applications requiring accurately flux-calibrated spectra over long wavelength baselines. However, the flux calibration in the mid-optical, e.g., 5000–7000 Å, should be less affected by the ADC problem and may be useful. Line indices in this wavelength range should be robust, as should flux ratios of lines of comparable wavelength (e.g., $[\text{O III}\lambda 5007]/\text{H}\beta$, $\text{H}\alpha/[\text{N II}\lambda 6585]$). Moreover, the ADC problems do not strongly effect the primary focus of measuring redshifts from the spectra.

3.4. Redshift Measurements

We measured redshifts from the MMT/Hectospec spectra using first an automated pipeline analysis, converted from the SDSS pipeline. We subsequently inspected each spectrum to check the automated measurement. The observing program was highly efficient: of the 1291 science targets for spectroscopy, we measured redshifts successfully for 1270 (a 98% success rate; including both those classified from the automated pipeline and those visually identified).

For our automated measurements, we used a version of the SDSS pipeline `specBS` (D. Schlegel et al. 2006; <http://spectro.astro.princeton.edu>) adapted for MMT/Hectospec for the AGN and Galaxy Evolution Survey (AGES) of the NDWFS in the constellation Boötes (Kochanek et al. 2006) and included in the HSRED package (see § 3.2). `SpecBS` uses χ^2 minimization to compare each spectrum to various model spaces, each a linear combination of eigentemplates at different redshifts. The minimum χ^2 yields the object’s spectral classification (star, galaxy, QSO, and any sub-classification) as well as the redshift. The classifications are included in table 5. The pipeline also provides a warning flag for the redshift (see § 5).

We then visually inspected the spectra to verify the accuracy of the pipeline-derived redshifts. The automated classification scheme had a high success rate: of the 1291 scientific objects we targeted with fibers, we found that the automated classification algorithm returned faulty or dubious redshifts in only 74 cases (5%). Most of these cases occur in observations at high airmass, where the spectra typically have excessive blue-light flux (see § 3.3). Roughly 50% (36/74) of objects with erroneous redshifts are from field 132 (airmass 1.35). The remaining erroneous redshifts are split fairly evenly between the three configurations taken at moderate airmass (131, 133, and 135). We found only five erroneous redshifts in field 134, with airmass 1.16.

For the majority of spectra with erroneous redshifts (53/74), we identified an alternative redshift by visual inspection. We then remeasured a redshift by fitting a Gaussian to the centroid of strong features in the spectra (normally $[\text{O II}]$ or $[\text{H}\alpha]$, depending on the redshift coverage, and in some cases the Ca H+K doublet) and corrected these to the heliocentric frame. We inserted these remeasured redshifts and uncertainties into the MMT/Hectospec catalog, and set `ZVISUALFIXFLAG=1` for these. For these objects, we visually identified the spectroscopic classification as either “Galaxy”, “QSO”, or “STAR”. Note that like SDSS, “QSO” refers to broad-line QSOs; objects identified as a “Galaxy” include also sources that may have putative narrow-line AGN based on broad $[\text{O III}]$, $\text{H}\alpha$, or line ratios. We also updated the spectroscopic subclassification to “manual” for objects where we remeasured the redshift.

Table 5 lists Hectospec spectroscopic results, including the automated redshifts, redshift uncertainty (columns 10–11), and spectroscopic classification and any subclassification (columns 8 and 9). These entries include objects where we manually measured the redshift, and modified the spectroscopic classification.

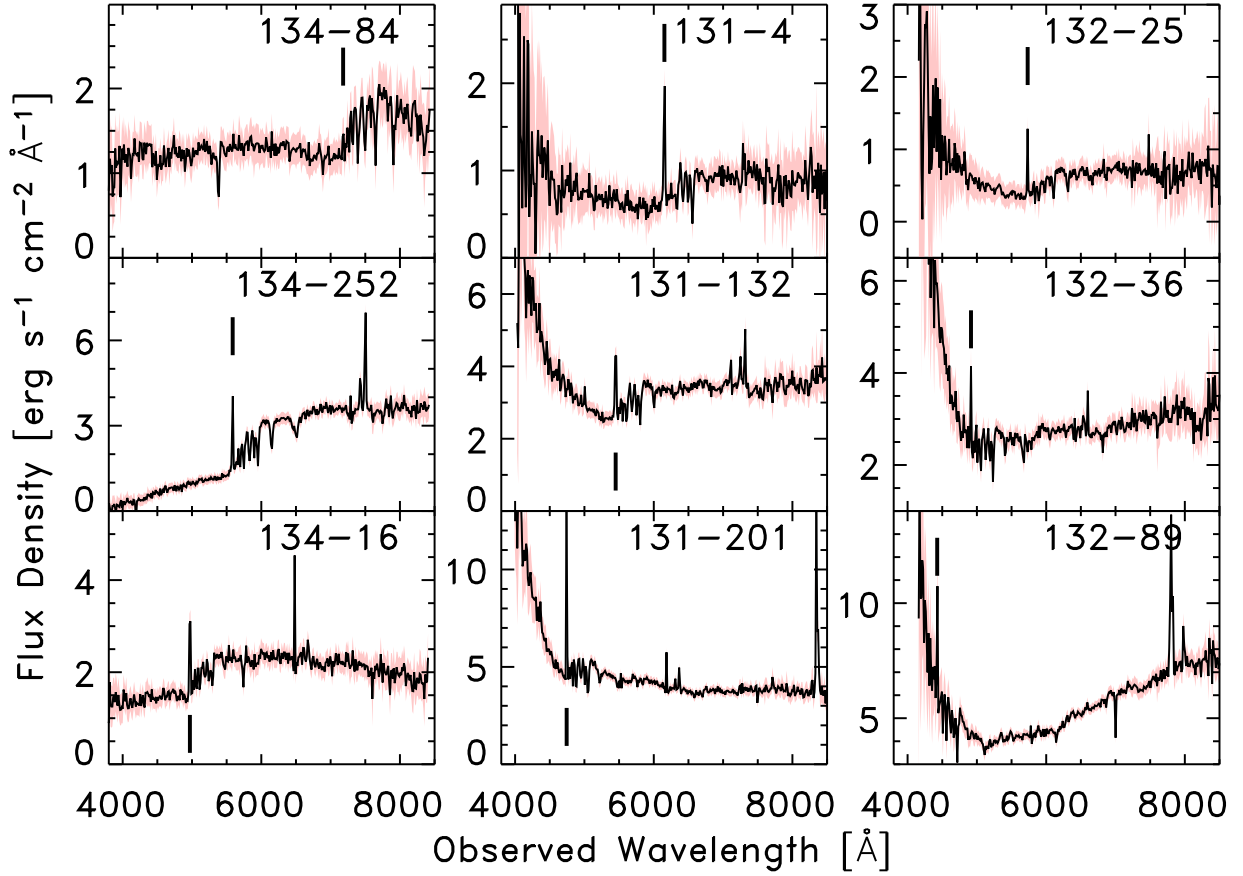


Fig. 4.— Example spectra from the Hectospec data, illustrating the problem with the atmospheric dispersion corrector. Each panel shows the flux-calibrated spectrum (heavy, black line; resampled to $R \sim 400$ and interpolated over pixels with bad mask values) for a source denoted by its Hectospec field and fiber number. The red, shaded region denotes the 1σ uncertainty. The heavy vertical lines denotes the observed wavelength of the [O II] $\lambda 3727$ line. The panels are ordered from left to right with increasing airmass at the time the field was observed (see table 2). The increase in flux density at the blue end of the spectrum illustrates the ADC-induced problem with the flux calibration.

Objects with visual-flag values of 1 (column 14) correspond to those we judged to have secure redshifts. Although we trust all objects with visual-flag values of 1, for completeness we include the redshift warning flag (ZWARNING; column 12), and reduced χ^2 of the redshift fit (column 13) from the automated measurement. We consider objects with visual-flag values of 0 to have untrustworthy redshifts, although we have left the pipeline-derived redshift in the catalog for completeness. Column 4 gives the field number from table 2 of the observation, column 5 gives the Hectospec number of the fiber used to target the object, and column 6 gives the reduction number. The ID numbers in table 5 column 1 correspond to the ID numbers in column 1 of table 3. Most of the objects with visual-flag values of 1 have good automated redshift measurements (with ZWARNING=0; column 12), but 63 of these objects have ZWARNING>0. Many of the ZWARNING >0 objects have high signal-to-noise spectra, although some (31/63) are ones for which we identified an alternative redshift. Objects with fix-flag values of 1 (ZVISUALFIXFLAG; column 15) correspond to objects for which we visually remeasured an alternative redshift as described above.

As part of the electronic edition of this publication, we present the full photometry and redshift catalog in three separate files. The pertinent information in these three files is given in tables 3–5. The photometry file contains astrometry and photometry from SDSS and MIPS for objects in a parent sample that includes all MIPS sources in the FLS with SDSS matches at $i < 21$ mag, 37 calibration stars, and 31 other targets that we observed on these configurations as filler targets (see below). Two other files contain the spectroscopic results from the MMT and from the SDSS, respectively. These three files are row synchronous; each file contains 7226 objects, including the 5698 objects in the primary, secondary, and tertiary samples. The ID numbers in column 1 of tables 3–5 correspond to the row of the object in each of the three catalog files.

4. Spectroscopic Completeness

As discussed in § 2.3, our targeting criteria select $\approx 60\%$ of all $24\ \mu\text{m}$ sources with $f_\nu(24\mu\text{m}) \geq 1$ mJy, and $\approx 30\%$ of those sources with $0.3\ \text{mJy} \leq f_\nu(24\mu\text{m}) < 1$ mJy. We did not observe MIPS $24\ \mu\text{m}$ sources with optical magnitudes fainter than $i > 21$ and 20.5 mag for the primary and secondary samples, respectively.

The total spectroscopic success rate is high. We define the redshift-success rate as the ratio of the number of Hectospec targets with measured redshifts to the number of Hectospec targets observed, which we show in figure 5. The redshift success rate for both the primary and secondary samples is 98–99% (599/605 targeted primary sources, and 619/632 targeted secondary sources have successfully measured redshifts).

We compute the overall spectroscopic completeness as the ratio of targets with successfully measured redshifts (including both the MMT/Hectospec and SDSS spectroscopy) to the subsample of targets in the parent sample that fall within our Hectospec fields, i.e., including only those objects that were targets or potential targets for our configurations. Figure 5 shows the spectroscopic completeness as a function of $24\ \mu\text{m}$ flux density. Objects without measured redshifts are counted once for each Hectospec field in which they occur (see figure 3). There are 820 objects in the primary sample falling in the region observed with Hectospec. Of these, 739 have redshifts, with 140 from the SDSS and 599 from our Hectospec program. This is a completeness of 90%. The 10% that were not observed tend to be near the outer edge of the observed region (see fig 3). Hectospec fibers extend nearly radial from the edge of the field of view, and near the edge only one fiber can serve a target, leading to diminishing completeness. Pairs closer than the minimum Hectospec fiber approach of $20''$ will also have only one object observed, unless one of the objects was bright enough to be observed by SDSS or unless the pair falls in the overlap region of two MMT pointings. Aside from these minor issues, the primary sample completeness does not have any significant spatial biases.

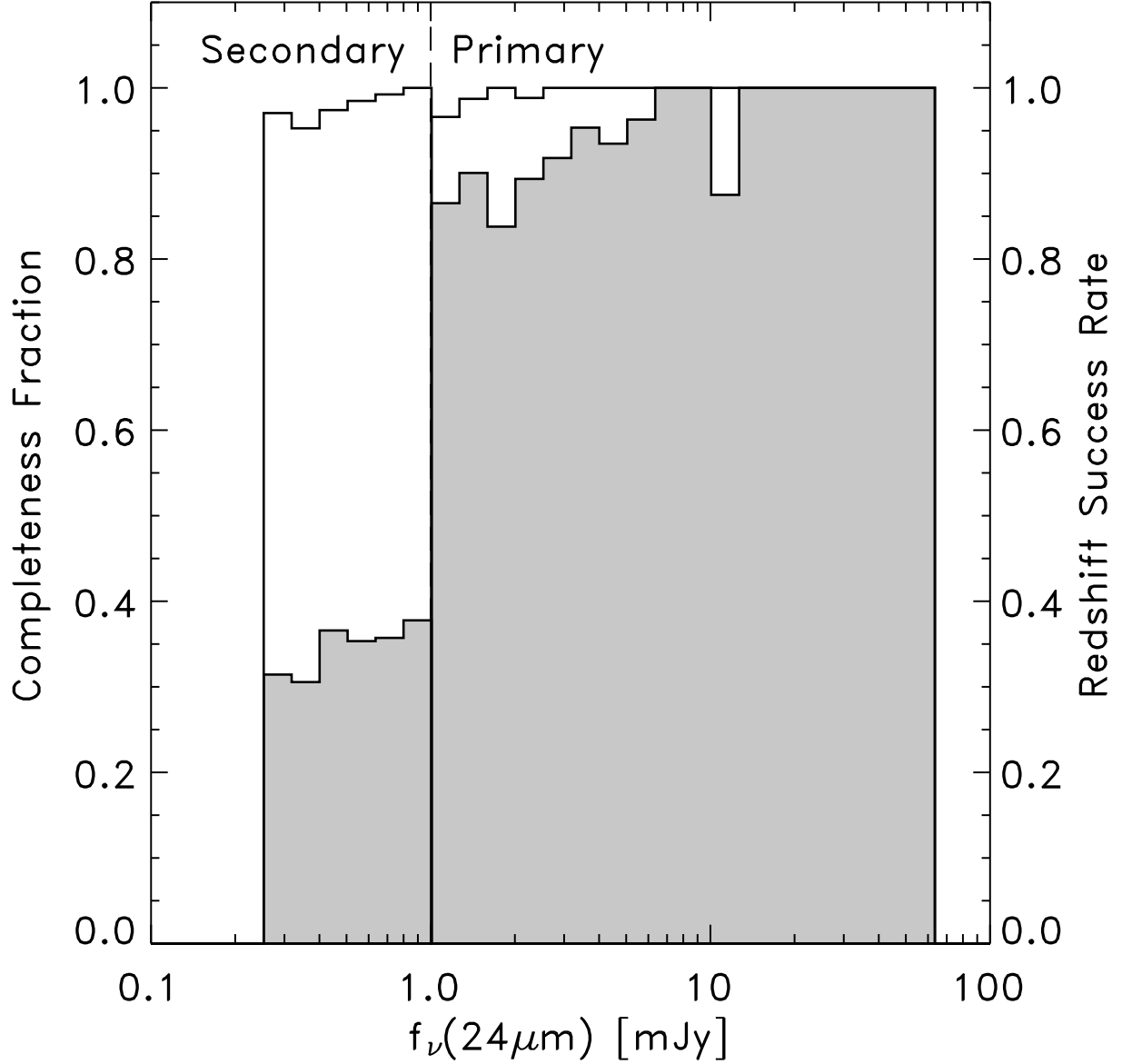


Fig. 5.— The completeness of the SDSS-matched $24\ \mu\text{m}$ spectroscopic sample as a function of $24\ \mu\text{m}$ flux density. The filled histograms show the completeness fraction of SDSS-matched $24\ \mu\text{m}$ sources with successfully measured redshifts (either from Hectospec or SDSS) to the total number of sources in each sample in the Hectospec region. The unfilled histogram shows the redshift–success rate, defined as the number of sources with successfully measured redshifts to the number of sources observed by Hectospec in each sample. The vertical dashed line delineates the primary and secondary samples (as labeled). The tertiary sample has low completeness ($<3\%$), and we do not show it here.

Of the 1771 objects in the secondary sample falling in the observed region, 662 have redshifts, with 43 from the SDSS and 619 from our Hectospec program (37% completeness). However, we stress that this completeness is highly spatially biased. One can clearly see large-scale structure in the sample that is not being tracked by the subset with spectra. We have not modeled this incompleteness yet, and one should be cautious about using the secondary sample for statistical applications that would be affected by a sampling that depends on the density of targets on the sky.

The tertiary sample is very sparsely covered ($< 3\%$ complete) and should not be used for statistical work.

5. The MMT/Hectospec Spectra

As part of this publication, we make available the fully reduced individual MMT/Hectospec spectra. These data are included as multi-extension FITS (MEF) files as part of the electronic edition of this publication. They are also available through the NASA/IPAC Infrared Science Archive (IRSA; see url in footnote 5). The format of the MEF files for the spectra is similar to those from the SDSS pipeline (<http://spectro.astro.princeton.edu>). There are 10 Header Data Unit (HDU) extensions in each MEF. Extensions 1–5 contain information for the spectra; these have dimension of $N_{\text{pixel}} \times N_{\text{fiber}}$, where $N_{\text{pixel}} = 4608$ is the number of pixels in the spectrum from each fiber and $N_{\text{fiber}} = 300$ is the number of fibers. Extension 6 contains targeting information for each fiber. Extensions 7–10 contain information on the flat field and sky spectrum from the data reduction. They are not useful for most applications. The HDUs are:

- HDU 1: Wavelength Solution in Ångstroms in vacuum;
- HDU 2: Flux density of the spectrum in units of $10^{-17} \text{ erg s}^{-1} \text{ cm}^{-2} \text{ Å}^{-1}$;
- HDU 3: Inverse variance (σ^{-2}) for the flux density;
- HDU 4: Mask of warning flags in each pixel combined between all exposures with logical AND;
- HDU 5: Mask of warning flags in each pixel combined between all exposures with logical OR;
- HDU 6: Structure containing targeting information for each fiber, it contains:
 - OBJTYPE: Type of fiber assignment (target, sky, standard star, or rejected);
 - RA: Right Ascension of fiber (deg; J2000);
 - DEC: Declination of fiber (deg; J2000);
 - FIBERID: Maps aperture to physical fiber on Hectospec;
 - RMAG: SDSS r -band magnitude of source;
 - RAPMAG: Estimate of the r -band magnitude measured through an aperture with $1''.5$ diameter;
 - ICODE: Integer targeting flags for the observation;
 - RCODE: Not used;
 - BCODE: Not used;
 - MAG: SDSS magnitudes for objects with OBJTYPE equal to standard star;
 - XFOCAL: x -coordinate of fiber on Hectospec focal plane;

- YFOCAL: y -coordinate of fiber on Hectospec focal plane;
 - FRAMES: Bookkeeping value from reductions;
 - EXPID: Name of highest-quality exposure;
 - TSOBJID: Not used;
 - TSOBJ_MAG: Bookkeeping values used in spectra flux calibration;
 - EBV_SFD: Galactic extinction, $E(B - V)$, for fiber derived from Schlegel, Finkbeiner, & Davis (1998).
- HDU 7: Structure containing B-Spline parameters for the sky spectrum derived for fibers 1–150;
 - HDU 8: Array of dimension $N_{\text{pixel}} \times 150$ containing the auxiliary flat-field correction derived for fibers 1–150 based on strength of sky lines as part of the reduction;
 - HDU 9: Same as HDU 6, but for fibers 151–300;
 - HDU 10: Same as HDU 8, but for fibers 151–300.

We remind the reader here that the flux calibration suffers from problems arising from the ADC (see § 3.3); caution should be used when using these spectra for applications required accurate flux calibration. The field and fiber value for each object in table 5 correspond to the array for each fiber in MEF for each field.

The data files also contain spectra of 57 objects not part of the MIPS sample. Of these, 26 are calibration stars; the other 31 are from a filler sample of $z \sim 0.5$ red galaxies and quasars, which are far too sparse to be statistically useful.

6. Discussion and Summary

We have obtained 1296 redshifts for *Spitzer* 24 μm -selected sources in the *Spitzer* FLS using the Hectospec fiber spectrograph on the MMT. Our observing program was highly efficient ($\simeq 98$ –99% redshift success rate). It is 90% complete for $f_{\nu}(24\mu\text{m}) \geq 1$ mJy and $i \leq 21$ mag, and is 37% complete for 0.3 mJy $< f_{\nu}(24\mu\text{m}) < 1$ mJy and $i \leq 20.5$ mag. As part of this publication we provide catalogs for the full parent sample, and the SDSS and MMT redshift catalogs. We also publish our reduced, flux-calibrated spectroscopic Hectospec data.

Our spectroscopic survey of the *Spitzer* FLS identifies galaxies and QSOs over a large redshift range. Figure 6 shows the redshift distribution for the 24 μm sources from the primary, secondary, and tertiary samples in the FLS, including 1246 sources identified as galaxies and QSOs from our MMT/Hectospec survey, and 280 additional galaxies and QSOs with redshifts from SDSS. Our Hectospec survey of 24 μm sources identifies galaxies to $z \leq 0.98$ and QSOs to $z \leq 3.6$. In figure 7, we show the MMT/Hectospec spectra of the highest redshift objects spectroscopically classified as a galaxy and QSO.

The redshift distribution for galaxies spans $0.01 \lesssim z_{\text{gal}} \lesssim 1$, and the distribution for QSOs extends to higher redshift $0.1 \lesssim z_{\text{QSO}} \lesssim 5$. The mean redshifts for galaxies and QSOs (including the Hectospec and SDSS data) are $\langle z_{\text{gal}} \rangle = 0.28$ and $\langle z_{\text{QSO}} \rangle = 1.1$, with standard deviations of $\sigma_{\text{gal}} = 0.17$ and $\sigma_{\text{QSO}} = 0.84$. For the primary sample, the mean redshifts for galaxies and QSOs are $\langle z_{\text{gal}} \rangle = 0.24$ and $\langle z_{\text{QSO}} \rangle = 1.0$, with standard deviations of $\sigma_{\text{gal}} = 0.17$ and $\sigma_{\text{QSO}} = 0.77$. Similarly, for the secondary sample, the mean redshifts

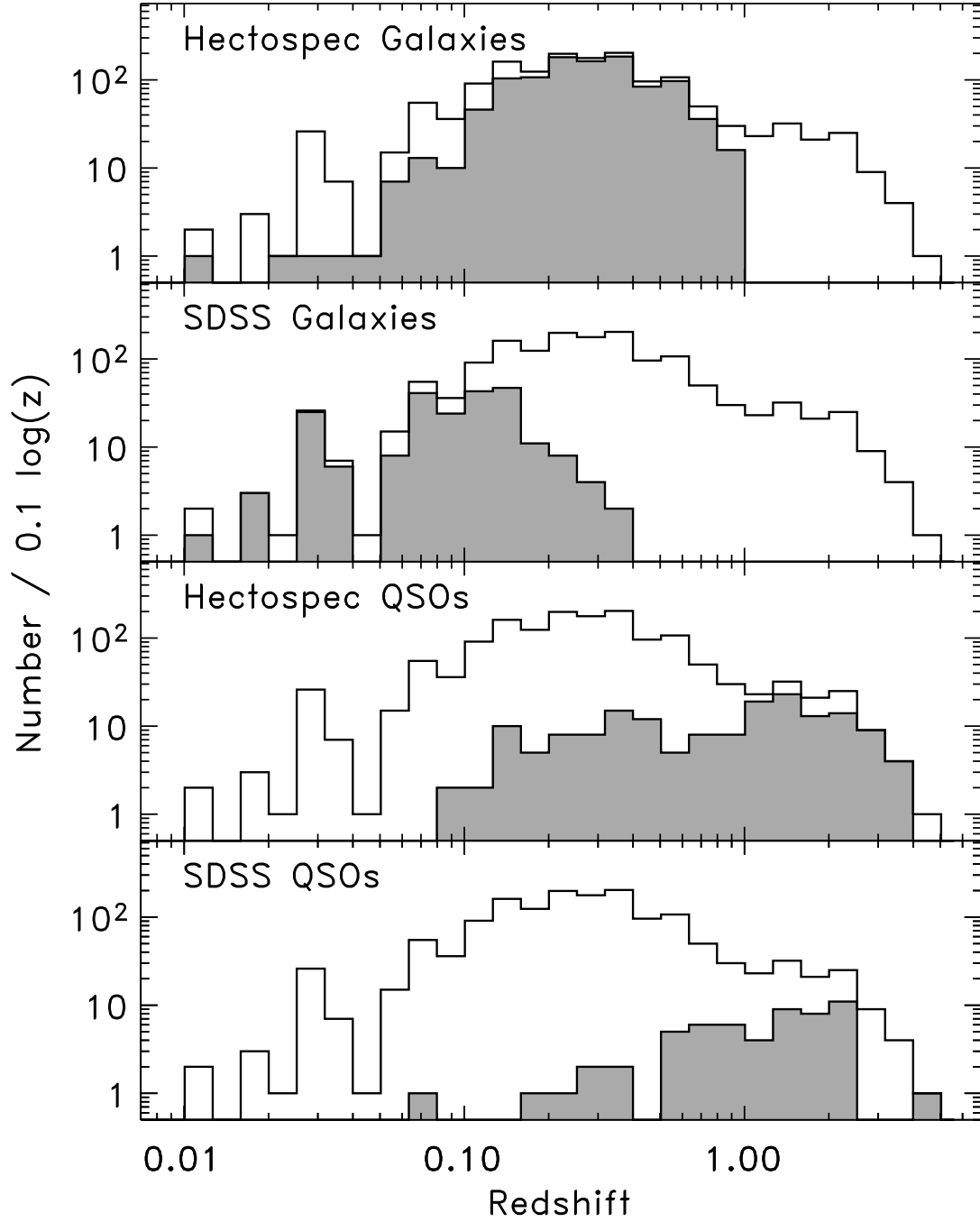


Fig. 6.— Redshift distribution of $24\ \mu\text{m}$ sources from the combined primary, secondary, and tertiary samples in the *Spitzer* FLS. In each panel, the shaded histogram shows the redshift distribution (as labeled) of sources spectroscopically classified as “Galaxies”, and “QSOs” from the Hectospec and SDSS data. The solid line shows the redshift distribution of all the MIPS samples from the Hectospec and SDSS samples.

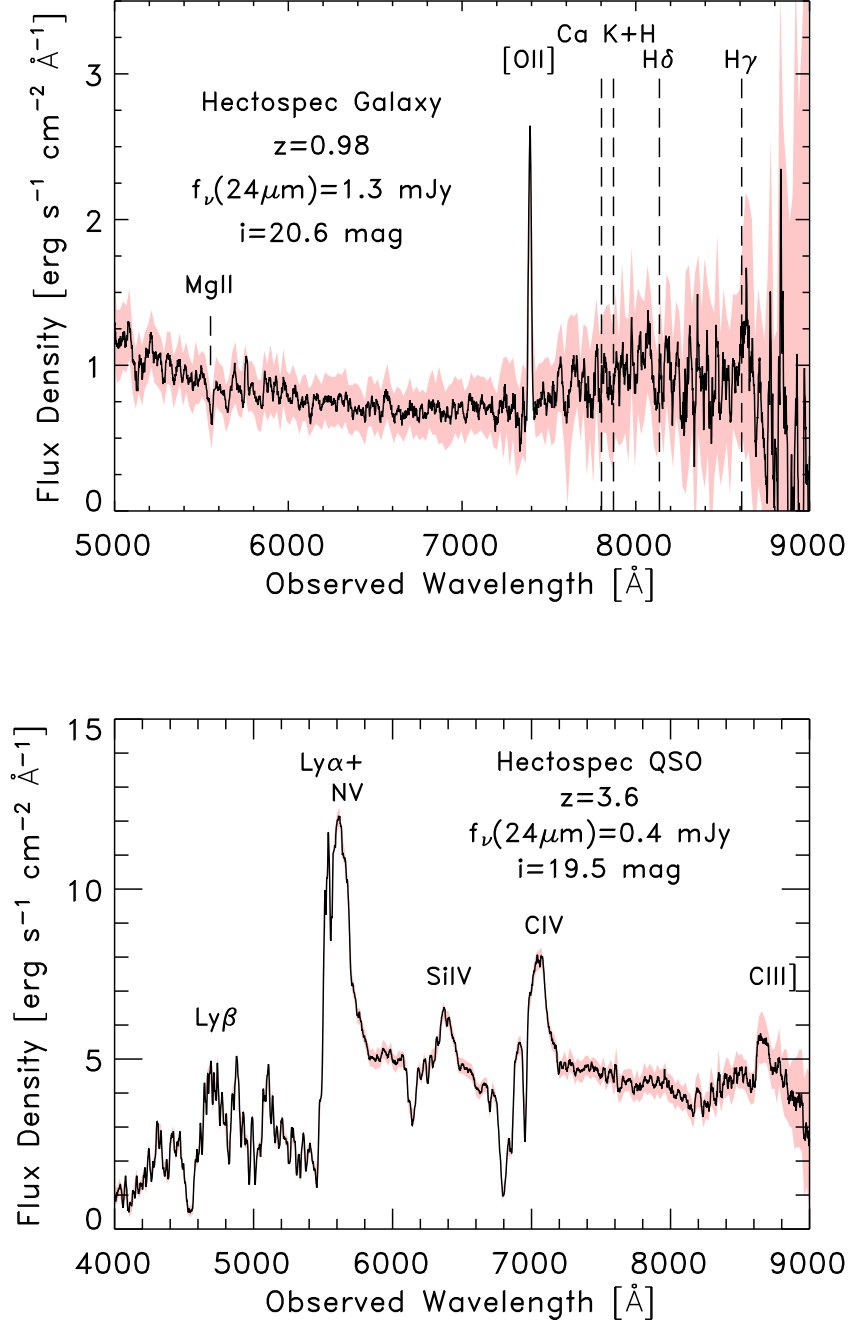


Fig. 7.— Objects classified as a galaxy and QSO with the highest redshift in the Hectospec data. In each panel, the black, solid line shows the reduced, flux-calibrated Hectospec spectrum (resampled to $R \sim 350$), and the red, shaded region shows the 1σ uncertainty. Locations of prominent features are labeled. Redshift, $24 \mu\text{m}$ flux density, and i -band magnitude are inset in each panel.

for galaxies and QSOs are $\langle z_{\text{gal}} \rangle = 0.31$ and $\langle z_{\text{QSO}} \rangle = 1.5$, with standard deviations of $\sigma_{\text{gal}} = 0.16$ and $\sigma_{\text{QSO}} = 0.94$.

The photometric and redshift catalogs, and reduced spectra are available with the electronic edition of this publication. They are also available through the NASA/IPAC Infrared Science Archive (IRSA; see footnote 5). We are currently pursuing further redshift surveys in *Spitzer* fields, building the datasets needed to understand the IR-active galaxy population.

We wish to thank Tom Soifer and the SSC staff for initiating the FLS project, and for their hard work processing the *Spitzer* data. We thank Michael Cushing, John Moustakas, and J. Davy Kirkpatrick for useful conversations and feedback, and we thank Lisa Storrie-Lombardi, Anastasia Alexov, Bruce Berriman, and J. Davy Kirkpatrick for their assistance in providing the data products through IRSA. We are grateful to the referee, Bahram Mobasher, for useful comments and suggestions. We thank the Hectospec instrument and queue-mode scientists and the MMT operators for their excellent assistance with the observations. Observations reported here were obtained at the MMT Observatory, a joint facility of the University of Arizona and the Smithsonian Institution. This work is also based in part on archival data obtained with the Spitzer Space Telescope, which is operated by the Jet Propulsion Laboratory (JPL), California Institute of Technology (Caltech) under a contract with NASA. Support for this work was provided by awards issued by JPL/Caltech, and by NASA through the Spitzer Space Telescope Fellowship Program, through a contract issued by JPL, Caltech under a contract with NASA.

This paper made use of data from the SDSS. Funding for the SDSS has been provided by the Alfred P. Sloan Foundation, the Participating Institutions, the National Aeronautics and Space Administration, the National Science Foundation, the U.S. Department of Energy, the Japanese Monbukagakusho, and the Max Planck Society. The SDSS Web site is <http://www.sdss.org/>. The SDSS is managed by the Astrophysical Research Consortium (ARC) for the Participating Institutions. The Participating Institutions are The University of Chicago, Fermilab, the Institute for Advanced Study, the Japan Participation Group, The Johns Hopkins University, the Korean Scientist Group, Los Alamos National Laboratory, the Max-Planck-Institute for Astronomy (MPIA), the Max-Planck-Institute for Astrophysics (MPA), New Mexico State University, University of Pittsburgh, University of Portsmouth, Princeton University, the United States Naval Observatory, and the University of Washington.

REFERENCES

- Abazajian, K., et al. 2004, *AJ*, 128, 502
- Bertin, E., & Arnouts, S. 1996, *A&A*, 117, 393
- Calzetti, D., et al. 2005, 633, 871
- Dole, H., et al. 2006, *A&A*, in press (astro-ph/0603208)
- Elbaz, D., Cesarsky, C. J., Chanial, P., Aussel, H., Franceschini, A., Fadda, D., & Chary, R. R. 2002, *A&A*, 384, 848
- Elbaz, D., et al. 1999, *A&A*, 351, L37
- Fabricant, D. et al. 2005, *PASP*, 117, 1411

- Gordon, K., et al. 2005, *PASP*, 117, 503
- Hauser, M. G., et al. 1998, *ApJ*, 508, 25
- Houck, J. R., et al. 2005, *ApJ*, 622, L105
- Kochanek, C. et al. 2006, in preparation
- Kurucz, R. L. 1993, *Kurucz CD-ROM*, Cambridge, MA: Smithsonian Astrophysical Observatory
- Le Floch, E., et al. 2005, *ApJ*, 632, 169
- Marleau, F. R., et al. 2004, *ApJS*, 154, 66
- Morton, D. C. 1991, *ApJS*, 77, 119
- O'Donnell, J. E. 1994, *ApJ*, 422, 158
- Oke, J. B., & Gunn, J. E. 1983, *ApJ*, 266, 713
- Papovich, C., & Bell, E. F. 2002, *ApJ*, 579, L1
- Papovich, C., et al. 2004, *ApJS*, 154, 70
- Pérez-González, P. G., et al. 2005, *ApJ*, 630, 82
- Pindor, B., Turner, E. L., Lupton, R. H., & Brinkmann, J. 2003, *AJ*, 125, 2325
- Rieke, G. H., et al. 2004, *ApJS*, 154, 25
- Roussel, H., Sauvage, M., Vigroux, L., & Bosma, A. 2001, *A&A*, 372, 427
- Schlegel, D. J., Finkbeiner, D. P., & Davis, M. 1998, *ApJ*, 500, 525
- Schlegel, D., et al. 2006, in preparation
- Soifer, B. T., Neugebauer, G., & Houck, J. R. 1987, *ARA&A*, 25, 187
- Soifer, B. T. & Neugebauer, G. 1991, *AJ*, 101, 354
- Spinoglio, L., Malkan, M. A., Rush, B., Carrasco, L., & Recillas-Cruz, E. 1995, *ApJ*, 453, 616
- Stoughton, C., et al. 2002, *AJ*, 123, 485
- Szentgyorgyi, A. H., Cheimets, P., Eng, R., Fabricant, D. G., Geary, J. C., Hartmann, L., Pieri, M. R., & Roll, J. B. 1998, *Proc. SPIE*, 3355, 242
- van Dokkum, P. G. 2001, *PASP*, 113, 1420
- Weedman, D. W., Le Floch, E., Higdon, S. J. U., Higdon, J. L., & Houck, J. R. 2006, *ApJ*, 638, 613
- Yan, L., et al. 2005, *ApJ*, 628, 604
- York, D. G., et al. 2000, *AJ*, 120, 1579

Table 1. Main SExtractor Parameters for the 24 μm Catalog

Parameter	Value
DETECT_MINAREA	3.0
DETECT_THRESH	2.5
FILTER	No
DEBLEND_NTHRESH	64
DEBLEND_MINCONT	0.02
CLEAN	Yes
CLEAN_PARAM	1.0
BACK_SIZE	50
BACK_FILTERSIZE	1

Table 2. Target Hectospec Fields

Field	R.A. (J2000)	Decl. (J2000)	t_{exp} (min)	Observation Date (UTC)	Airmass
131	17 14 19.5	+59 51 29	45	2004 Jun 13	1.23
132	17 19 59.1	+59 52 10	45	2004 Jun 13	1.35
133	17 12 54.9	+59 03 24	45	2004 Jun 15	1.23
134	17 18 16.6	+59 01 48	45	2004 Jun 20	1.16
135	17 23 57.6	+58 55 59	45	2004 Jun 23	1.26

Note. — Units of right ascension are hours, minutes, and seconds, and units of declination are degrees, arcminutes, and arcseconds.

Table 3. SDSS–Matched 24 μm Catalog

ID (1)	R.A. (J2000) (2)	Decl. (J2000) (3)	i (mag) (4)	$u-g$ (mag) (5)	$g-r$ (mag) (6)	$r-i$ (mag) (7)	$i-z$ (mag) (8)	$A(r)$ (mag) (9)	Targ. Flag (10)	$\log f_\nu(24\mu\text{m})$ (mJy) (11)	SNR ₂₄ (12)	R.A. (24 μm) (J2000) (13)	Decl. (24 μm) (J2000) (14)
1	17 17 50.52	+60 26 48.1	18.01	1.30	0.50	0.15	0.03	0.066	8	−1.33	0.98	17 17 50.40	+60 26 47.9
2	17 17 55.48	+60 26 39.3	17.59	1.92	1.28	0.50	0.32	0.066	4	−0.15	3.51	17 17 55.53	+60 26 39.6
3	17 18 02.38	+60 27 20.8	18.60	1.09	1.36	0.51	0.27	0.067	8	−0.74	2.29	17 18 02.35	+60 27 20.7
4	17 17 53.86	+60 26 20.2	20.36	2.54	0.91	0.40	0.46	0.065	4	−0.40	2.58	17 17 54.02	+60 26 21.3
5	17 18 11.89	+60 26 49.3	20.19	1.71	1.50	0.39	0.52	0.066	4	−0.39	2.58	17 18 11.89	+60 26 49.3
6	17 17 30.78	+60 26 37.6	20.84	−0.25	1.59	0.48	0.28	0.066	0	−0.87	1.46	17 17 30.95	+60 26 36.6
7	17 18 11.34	+60 27 06.9	20.53	1.31	1.53	0.65	0.69	0.066	0	−0.57	2.71	17 18 11.33	+60 27 06.4
8	17 18 21.07	+60 27 29.3	20.87	1.81	1.67	0.41	0.24	0.066	0	−1.37	1.08	17 18 21.08	+60 27 27.5
9	17 18 37.32	+60 25 24.6	19.92	3.51	0.98	0.41	0.28	0.063	8	−1.05	1.25	17 18 37.49	+60 25 24.2
10	17 17 50.77	+60 17 01.2	16.02	1.95	0.90	0.38	0.31	0.057	8	−1.22	0.94	17 17 50.86	+60 17 01.9
11	17 18 20.37	+60 26 20.8	20.65	0.75	1.02	0.49	0.43	0.065	0	−0.34	3.10	17 18 20.41	+60 26 21.1
12	17 18 44.49	+60 23 42.3	18.65	0.74	0.95	0.35	0.36	0.062	2	0.62	11.85	17 18 44.56	+60 23 41.8
13	17 18 31.60	+60 21 00.7	17.29	1.72	1.08	0.52	0.41	0.059	2	0.04	5.31	17 18 31.63	+60 21 00.8
14	17 18 33.48	+60 26 16.9	20.96	1.42	1.31	0.44	0.24	0.065	0	−0.56	2.47	17 18 33.52	+60 26 15.6
15	17 17 41.68	+60 25 14.3	17.98	1.18	0.52	0.30	0.12	0.064	8	−0.69	2.06	17 17 41.63	+60 25 13.0
16	17 17 34.21	+60 23 50.7	19.01	0.27	0.49	0.35	0.27	0.062	2	0.20	6.64	17 17 34.23	+60 23 52.0
17	17 17 50.54	+60 23 29.5	19.15	0.61	0.66	0.30	0.04	0.060	4	−0.34	2.83	17 17 50.67	+60 23 29.3
18	17 18 41.06	+60 23 59.1	19.54	0.24	0.22	0.35	0.10	0.062	2	0.02	5.47	17 18 41.09	+60 23 58.5
19	17 18 47.92	+60 24 09.4	18.73	1.28	1.16	0.34	0.41	0.062	4	−0.10	4.31	17 18 47.94	+60 24 09.7
20	17 18 47.42	+60 23 30.9	19.55	0.35	1.13	0.38	0.30	0.062	4	−0.25	3.04	17 18 47.62	+60 23 30.4

Note. — (1) Row synchronous ID; (2) SDSS right ascension in units of hours, minutes, and seconds; (3) SDSS declination in units of degrees, arcminutes, and arcseconds; (4) SDSS combined–model magnitude (dereddened); (5–8) SDSS combined–model colors (dereddened); (9) Extinction used to deredden magnitudes in (4–8); (10) Hectospec Target Flag (see text); (11) Logarithm of MIPS 24 μm flux density; (12) MIPS 24 μm signal–to–noise ratio, $\equiv f_\nu(24\mu\text{m})/\delta f_\nu(24\mu\text{m})$; note that 24 μm flux–density errors do not include correlated pixel noise and are thus underestimated (see text); (13) right ascension of MIPS 24 μm source in units of hours, minutes, and seconds; (14) declinations of MIPS 24 μm source in units of degrees, arcminutes, and arcseconds. Table 3 is published in its entirety in the electronic edition of the *Astronomical Journal*. A portion is shown here for guidance regarding its form and content.

Table 4. SDSS–Spectroscopic Catalog

ID (1)	R.A. (J2000) (2)	Decl. (J2000) (3)	SDSS information			Targ. Code (7)	class (8)	subclass (9)	z (10)	$\sigma(z)$ (11)	Warn. (12)	χ^2/ν (13)
10	17 17 50.76	+60 17 01.4	354	262	51792	64	galaxy	...	0.07923	0.00002	0	1.31
67	17 18 15.67	+60 08 22.0	353	612	51703	64	galaxy	...	0.15671	0.00001	0	1.38
100	17 19 44.06	+60 02 44.6	354	298	51792	64	galaxy	...	0.09421	0.00001	0	1.20
107	17 18 53.16	+60 05 41.0	354	299	51792	64	galaxy	...	0.13285	0.00001	0	1.30
155	17 19 44.88	+59 57 06.9	354	290	51792	64	galaxy	...	0.06890	0.00001	0	1.34
159	17 20 07.90	+60 01 59.7	354	285	51792	64	galaxy	...	0.07541	0.00002	0	1.22
255	17 20 02.11	+59 42 40.8	353	628	51703	4	galaxy	...	0.23937	0.00000	0	1.73
256	17 19 44.14	+59 41 01.0	354	292	51792	64	galaxy	AGN	0.12926	0.00001	0	2.03
258	17 20 09.50	+59 40 30.1	354	289	51792	64	galaxy	...	0.02760	0.00001	0	1.55
324	17 20 47.14	+59 33 14.5	366	338	52017	96	galaxy	...	0.07041	0.00002	0	1.29
325	17 20 41.40	+59 32 44.3	353	636	51703	1048580	QSO	broadline	1.18430	0.00037	0	1.47
327	17 21 02.95	+59 33 12.9	353	634	51703	64	galaxy	...	0.07014	0.00001	0	1.49
369	17 20 02.83	+59 22 50.0	353	39	51703	0	star	F5	−0.00053	0.00002	0	1.15
374	17 20 19.94	+59 24 16.5	366	335	52017	64	galaxy	...	0.15423	0.00001	0	1.42
377	17 21 04.75	+59 24 51.4	366	334	52017	34603008	QSO	broadline	0.78576	0.00034	0	1.41
380	17 20 56.71	+59 19 36.8	366	382	52017	64	galaxy	...	0.06710	0.00001	0	1.33
381	17 21 28.70	+59 19 41.3	353	40	51703	64	galaxy	AGN	0.06544	0.00001	0	1.66
429	17 21 52.92	+59 11 55.5	366	385	52017	96	galaxy	...	0.06593	0.00001	0	1.54
430	17 20 45.22	+59 16 17.7	353	35	51703	64	galaxy	...	0.15352	0.00001	0	1.54
436	17 21 56.93	+59 13 57.2	366	390	52017	64	galaxy	...	0.06535	0.00001	0	1.26
437	17 20 55.01	+59 11 16.8	353	30	51703	64	galaxy	...	0.06581	0.00001	0	1.37

Note. — (1) Row synchronous ID; (2) SDSS right ascension of spectroscopic target in units of hours, minutes, and seconds; (3) SDSS declination of spectroscopic target in units of degrees, arcminutes, and arcseconds; (4) SDSS field; (5) SDSS fiber number; (6) SDSS reduction run; (7) SDSS primTarget code (decimal); (8) spectroscopic classification; (9) spectroscopic subclassification; (10) redshift; (11) redshift error; (12) redshift warning, =0 is safe value; (13) χ^2 per degree of freedom for fit. Table 4 is published in its entirety in the electronic edition of the *Astronomical Journal*. A portion is shown here for guidance regarding its form and content. The electronic version of this catalog includes an entry for each row in table 3, including null rows with no spectroscopic information.

Table 5. Hectospec–Spectroscopic Catalog

ID	R.A.			Decl.			Hectospec information			Targ.							
(1)	(J2000)			(J2000)			Field	Fiber	Rerun	Code	class	subclass	z	$\sigma(z)$	Warn.	χ^2/ν	Vis.
	(2)			(3)			(4)	(5)	(6)	(7)	(8)	(9)	(10)	(11)	(12)	(13)	Flag
																	(15)
54	17	18	24.87	+60	18	58.5	132	265	300	4	galaxy	...	0.40845	0.00011	0	1.63	1
61	17	18	23.47	+60	11	04.1	132	251	300	4	QSO	broadline	1.42971	0.00078	0	1.03	1
65	17	19	23.05	+60	13	16.4	132	36	300	2	galaxy	...	0.31870	0.00003	0	1.12	1
66	17	19	26.87	+60	13	03.7	132	38	300	2	galaxy	...	0.16146	0.00001	0	1.66	1
68	17	18	31.25	+60	08	32.1	132	255	300	4	star	manual	−0.00066	0.00011	0	0.91	1
72	17	19	01.99	+60	12	18.4	132	4	300	4	galaxy	...	0.17466	0.00004	0	1.53	1
74	17	18	41.04	+60	15	07.2	132	263	300	4	galaxy	manual	0.21740	0.00011	0	1.31	1
76	17	18	42.88	+60	10	00.9	132	266	300	4	galaxy	...	0.27900	0.00004	0	1.23	1
79	17	18	45.97	+60	17	06.5	132	2	300	2	galaxy	...	0.21761	0.00003	0	1.04	1
81	17	19	27.99	+60	17	17.6	132	39	300	4	galaxy	...	0.24725	0.00006	0	0.88	1
82	17	18	25.34	+60	14	11.3	132	268	300	4	galaxy	...	0.62651	0.00006	0	0.93	1
88	17	18	28.76	+60	11	00.3	132	262	300	2	galaxy	...	0.26943	0.00006	0	0.98	1
89	17	18	57.85	+60	10	58.0	132	261	300	4	galaxy	...	0.24753	0.00006	0	0.91	1
91	17	19	14.34	+60	10	42.0	132	8	300	2	galaxy	...	0.23165	0.00002	0	1.19	1
96	17	18	40.72	+60	07	25.6	132	253	300	1	star	F5	−0.00110	0.00001	0	3.15	1
98	17	18	43.49	+60	02	24.8	132	291	300	2	galaxy	...	0.13305	0.00001	0	2.84	1
99	17	18	42.16	+60	03	16.6	132	258	300	4	galaxy	...	0.12986	0.00002	0	1.05	1
104	17	18	24.77	+60	05	17.2	132	256	300	2	galaxy	...	0.12923	0.00001	0	5.08	1
109	17	18	57.82	+60	01	45.8	132	260	300	4	galaxy	...	0.18926	0.00003	0	0.96	1
112	17	19	28.74	+60	03	45.1	132	6	300	2	galaxy	...	0.20937	0.00003	0	1.02	1
113	17	19	46.96	+60	03	42.6	132	31	300	2	galaxy	...	0.27874	0.00001	0	1.09	1

Note. — (1) Row synchronous ID; (2) Hectospec right ascension of spectroscopic target in units of hours, minutes, and seconds; (3) Hectospec declination of spectroscopic target in units of degrees, arcminutes, and arcseconds; (4) Hectospec field; (5) Hectospec fiber number; (6) Hectospec reduction run; (7) Hectospec Target code (decimal); (8) spectroscopic classification; (9) spectroscopic subclassification; (10) redshift; (11) redshift error; (12) redshift warning, =0 is safe value, >0 is safe only if Visual flag in (14) is =1; (13) χ^2 per degree of freedom for fit. (14) Visual inspection flag, 1 indicates secure redshift, 0 indicates dubious or insecure redshift; (15) Flag indicates automatic redshift discarded and replaced (see text). Table 5 is published in its entirety in the electronic edition of the *Astronomical Journal*. A portion is shown here for guidance regarding its form and content. The electronic version of this catalog includes an entry for each row in table 3, including null rows with no spectroscopic information.